IV

Publication IV

Majander P., Siikonen T., Large-Eddy Simulation of a Round Jet in a Crossflow, Proceedings of the 4th ECCOMAS Congress on Computational Methods in Applied Sciences and Engineering, July 24-28 2004, Jyvaskylä.

© 2004 by authors

European Congress on Computational Methods in Applied Sciences and Engineering
ECCOMAS 2004
P. Neittaanmäki, T. Rossi, K. Majava, and O. Pironneau (eds.)
W. Rodi and P. Le Quéré (assoc. eds.)
Jyväskylä, 24–28 July 2004

LARGE-EDDY SIMULATION OF A ROUND JET IN A CROSSFLOW

Petri Majander and Timo Siikonen

Laboratory of Applied Thermodynamics, Helsinki University of Technology
P.O. Box 4400, FINLAND
e-mails: Petri.Majander@hut.fi, Timo.Siikonen@hut.fi

Key words: large-eddy simulation, jet in crossflow, parallel computation

Abstract. *A large-eddy simulation of a round jet penetrating normally into a crossflow is described. The jet-to-crossflow velocity ratio is 2.3 at a Reynolds number of 46 700, based on the jet bulk velocity and the jet diameter. The simulation is performed with a parallel pressure-based Navier-Stokes solver. The spatial discretization is based on a co-located and structured finite-volume technique and a body-fitted co-ordinate system. A domain decomposition technique and a message passing library (MPI) is utilized in the parallelization. The results are compared with experimental measurements. The computation reproduced many phenomena present in such a flow, like the shear layer ring vortices. In general, a reasonable agreement with the measurements was obtained. However, the calculation predicts the backflow too low near the flat wall and too close to the jet which is the most significant deviation from the measured flow.*

1 INTRODUCTION

Jets in a crossflow are complex flows with many practical applications ranging from jets into combustors to V/STOL aircraft in transition flight. Perhaps the most familiar example in everyday life would be smoke rising from a chimney into a crosswind. Due to the great practical relevance, many experimental, numerical and theoretical studies have been undertaken. Here only a few are cited. Keffer and Baines [6] measured the trajectory of the jet and the velocity along it. The turbulent intensity was also measured along a line in the plane orthogonal to the jet trajectory. A more complete survey was conducted by Crabb, Durão and Whitelaw [3] who measured mean and fluctuating velocity magnitudes with a laser-Doppler anemometer near the jet exit and hot wires further downstream. This flow is the subject of a simulation in the present research. Andreopoulos and Rodi [1] used a triple wire probe to simultaneously measure all three components of velocity. Kelso, Lim and Perry [7] studied the structure of round jets in crossflows using flow visualization techniques and flying-hot-wire measurements. The jet-to-crossflow velocity ratios ranged from 2 to 4 and the Reynolds numbers varied between 440 and 6200, based on the jet diameter and free-stream velocity.
Jets in a crossflow have also been studied numerically and here two examples are paid attention to. Yuan, Street and Ferziger [13] performed large-eddy simulations (LES) at two jet-to-crossflow velocity ratios, 2.0 and 3.3, and two Reynolds numbers, 1050 and 2100, based on the crossflow velocity and the jet diameter. They discretized the computational area into a total of 1.34×10^6 control volumes. The jet in a crossflow measured by Crabb et al. was modelled with LES by Wille [12]. He used both a coarse and a fine mesh, which included 88440 and 997920 mesh points, respectively. Considering the Reynolds number of 46 700, based on the jet bulk velocity and the jet exit diameter, both grids are quite coarse even if the near-wall boundary layers were modelled. In [12] it is not explicitly stated whether the Reynolds number is the same as in the experiment.

In this study a parallel solver developed at the laboratory of the Applied Thermodynamics in Helsinki University of Technology is used to compute an LES of a jet in a crossflow measured in [3] and a comparison to the experiment is carried out. In the next chapter, the governing equations and the numerical methods are presented. In Chapter 3, the characteristics of the computational case are described. The results are shown and compared to the measurements in Chapter 4, and finally in Chapter 5, the conclusions are drawn.

2 GOVERNING EQUATIONS

The filtered LES equations for isothermal incompressible flows with a passive scalar θ transport are written as

$$\frac{\partial \overline{u}_i}{\partial x_i} = 0 \tag{1}$$

$$\frac{\partial \overline{u}_i}{\partial t} + \frac{\partial \overline{u}_i \overline{u}_j}{\partial x_j} = -\frac{1}{\rho}\frac{\partial \overline{p}}{\partial x_i} + \frac{\partial}{\partial x_j}(\nu\ 2\ \overline{S}_{ij} - \tau_{ij}) \tag{2}$$

$$\frac{\partial \overline{\theta}}{\partial t} + \frac{\partial \overline{\theta} \overline{u}_j}{\partial x_j} = \frac{\partial}{\partial x_j}\left(\alpha \frac{\partial \overline{\theta}}{\partial x_j} - q_j\right), \tag{3}$$

where $\overline{u}_i$ are velocity components, $\overline{p}$ is pressure and ρ is a constant density. Molecular viscosity and diffusivity are denoted by ν and α. The strain rate tensor is

$$\overline{S}_{ij} = \frac{1}{2}\left(\frac{\partial \overline{u}_i}{\partial x_j} + \frac{\partial \overline{u}_j}{\partial x_i}\right). \tag{4}$$

The subgrid-scale stress and scalar flux are

$$\tau_{ij} = \overline{u_i u_j} - \overline{u}_i \overline{u}_j \tag{5}$$

$$q_j = \overline{\theta u_j} - \overline{\theta}\overline{u}_j, \tag{6}$$

respectively. The Boussinesq approximation

$$\tau_{ij} - \frac{\delta_{ij}}{3}\tau_{kk} = -2\nu_{sgs}\overline{S}_{ij} \tag{7}$$

relates subgrid-scale stresses τ_{ij} to the eddy viscosity ν_{sgs} and the resolved-scale strain rate tensor $\overline{S}_{ij}$. The Smagorinsky model for the eddy viscosity is written as

$$\nu_{sgs} = (C_s \Delta)^2 |\overline{S}|, \tag{8}$$

where C_s is called a Smagorinsky constant, Δ is a length scale and $|\overline{S}| = \sqrt{2\overline{S}_{ij}\overline{S}_{ij}}$ [11]. The length scale represents the cell size and it is usually computed as $V^{1/3}$. A value of 0.18 for C_s has been evaluated for the inertial range dynamics. In the presence of shear flow a smaller value must be used, which was first discovered by Deardorff [4]. He studied a channel flow and found that a smaller value for $C_s = 0.1$ had to be used in the presence of a strong shear-driven turbulence. This observation has since been confirmed by many studies. Furthermore, in the vicinity of the walls, the eddy viscosity is often reduced with the van Driest damping function. The subgrid-scale scalar flux is modelled analogously with a mixing length gradient model

$$q_j = -\frac{\nu_{sgs}}{Pr_{sgs}}\frac{\partial \overline{\theta}}{\partial x_j} \tag{9}$$

Depending on the flow, molecular Prandtl number Pr and the direction and the distance of the scalar flux to the wall, values for the turbulent Prandtl number Pr_{sgs} ranging from 0.3 to 0.8 have been presented [2].

3 FLOW SOLVER

The simulation is performed with a parallel SIMPLE-based Navier-Stokes solver developed at Laboratory of Applied Thermodynamics, Helsinki University of Technology. A body-fitted co-ordinate system is implemented with a co-located and structured finite-volume technique. Multi-block meshes are used to solve flows in complex domains. The parallelization takes advantage of the multi-block decomposition, each block is assigned to its own processor. The boundary values between the processes are exchanged with message passing library (MPI). For large-eddy simulation a second-order central difference is used for a spatial discretization and a second-order three-level implicit method for time stepping. Within a time step the solution is iterated. The Poisson equations for the momenta, pressure and scalars are solved in a series with an algebraic multigrid solver. Details of the method and validation benchmarks are available in [10] and [9].

4 FLOW CONFIGURATION

The setup of the jet in a crossflow is sketched in Fig. 1. The Reynolds number Re_D = 46 700 referred to the pipe flow is rather large for an LES of the whole jet. Therefore the computational domain has been reduced from that of the wind tunnel used by Crabb et al. [3]. The domain size used in [12] is $12D \times 6D \times 6D$ and it was suspected that the domain restricted the spreading of the jet, therefore the present domain is slightly larger. The number of the control volumes (CVs) is $192 \times 96 \times 144$ in streamwise, wall-normal and spanwise direction, respectively. In addition to this, a jet pipe is represented with 110 592 CVs, altogether 2 764 800 CVs, which are equally distributed into 25 blocks. The grid is clustered around the jet exit and the height of the first cell from the lower wall is $0.002D$, which corresponds to $\Delta y^+ = 4.7$ if scaled by the shear velocity of the incoming turbulent pipe flow. The stretching factor in the wall-normal direction is less than 1.06. Crabb et al. found that without the jet, the height of the boundary layer in front of the jet exit was about $0.24D$ high [3]. Here a uniform cross velocity U_∞ is set at the inlet. At the lateral and top surfaces free-slip boundary conditions are applied and a no-slip condition is forced at the bottom wall. At the outlet a zero-gradient (Neumann) condition (NBC) is used. The authors have compared the CBC with the NBC in a shedding cylinder flow. The CBC excelled over NBC only if the outlet boundary was located very close to the cylinder [8]. Wille used the CBC, but he found that there was virtually no effect on the predicted first and second moments, as the two conditions were tested with the plane jet in a crossflow [12].

A steady fully developed turbulent profile is prescribed at the lower end of the jet pipe, being one diameter below the wall. This allows the crossflow and the pipe flow to interact more realistically. Wille [12] defined the vertical velocity profile at the jet exit from the dynamic pressure and the tangential velocities were zero at the lower wall preventing the interaction. A zero-gradient pressure surrounds the whole area and the average pressure level in the area is fixed. Crabb et al. seeded the jet with helium trace and measured the

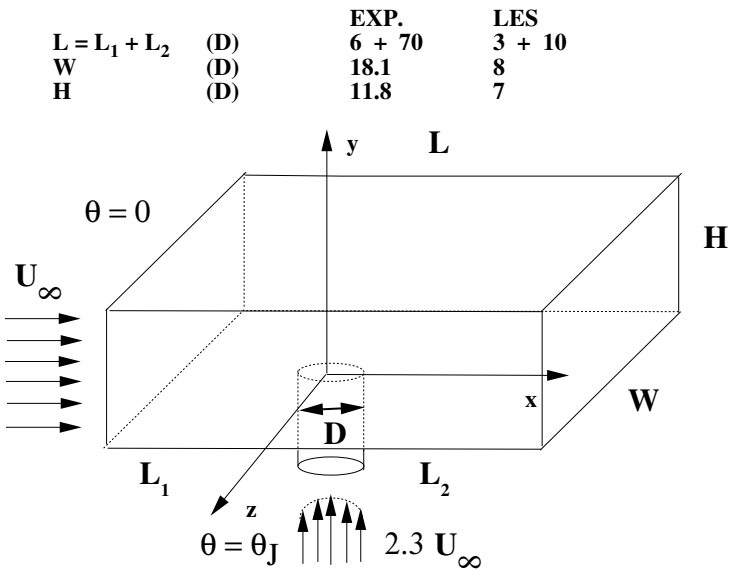

Figure 1: Schematics of the domain in the jet in a crossflow. The experiment refers to the windtunnel used by Crabb et al. [3] whereas the LES refers to the computational domain size.

mixture fraction θ/θ_J at different locations downstream. In the crossflow inlet $\theta/\theta_J = 0$ and in the jet $\theta/\theta_J = 1$. A zero-gradient for the scalar is set at all the other boundaries. Turbulent Prandt or Schmidt number was set to a constant value of 0.6.
The startup of the calculation was quite difficult. The dynamic model did not stabilize the computation and consequently it was not used. An excesssive value for the Smagorinsky constant C_s was set, until after some transient time, it was lowered to a value of 0.17. Also, an underrelaxation of a few per cent was added to the diagonal of the pressure correction equation in order for the MG solver to converge. The time step was rather short, $\Delta t = 0.005T$, where $T = D/2U_b$. This implies that the bulk crossflow advances from the inlet to the outlet during 5200 time steps. Due to the relatively thin cells the highest CFL -values are around 4 at the jet exit, however. A total of 15 subiterations was calculated during a time-step. It might have been possible to obtain the same results with a smaller amount of iterations, but this was not tested.The global mass balance residual reduced to a third from the first iteration, which is a rather poor convergence. Since the time step is globally so small, a global mass error remains small even at the first iteration cycle. In the beginning of the simulation, larger numbers of iterations within the time step were required for the stability. The flow was computed a time of 113 T from the initial state before statistics were gathered. After 200 T first results were reported. The calculation was continued until $t = 266T$. The results were relatively converged already at $t = 200T$, especially near the jet exit. The biggest differences were seen in non-diagonal stresses in the far field at $x/D = 8$. There was no need to reconsider the conclusions due to the continued computation, however. In calendar time all this corresponds to

approximately 40 days when using 25 Power4 processors of an IBM SP cluster.

5 RESULTS

5.1 Flow Field

In this section a qualitative overview on the flow field is given. The mean flow streamlines in the jet exit region are shown in Fig. 2. In the central plane upstream of the jet exit there is a single vortex (V_1), whose centre is located 0.25 D upstream of the lip. Kelso et al. found that at a smaller Reynolds number $U_\infty D/\nu = 1600$ there were two vortices in front of the jet, separated by a saddle point. They also visualized a 'hovering vortex' above the jet exit. The vortex originates from the collision of the jet and the crossflow shear layers. From Fig. 2 it is seen that in the present result there are three distinguishable roll-up vortices (V_2, V_3, V_4), two of them inside the pipe (V_3, V_4). Some part of the crossflow near the surface is swept into the pipe. The saddle point S, or the lowest point where the incoming fluid penetrates, is located at approximately y/D = -0.2. At a Reynolds number smaller by over a decade, and at the jet-to-crossflow velocity ratios $R = 2.2$ and 4.0, Kelso et al. reports the saddle point locations of y/D = -0.4 and -0.16, respectively. At high velocity ratios (≥ 6) the saddle point is located at the lip [7]. In the symmetry plane downstream of the jet, there resides a node (N) at $x/D = 1.03$ and $y/D = 0.17$. A vortex is also located right downstream of the jet exit edge (V_5). Behind the jet there is a rather strong backflow near the flat plate, confirmed by Fig. 3 which shows the contours of the mean streamwise and vertical velocity in the central plane. The backflow reaches a velocity of 0.8 times the free-stream value. The crossflow deflects over the bending jet and accelerates to a value of nearly twice its free-stream value. The mean vertical vertical velocity contours (Fig. 3) reveal two regions of strong upward motion. The upper region is generated directly by the jet. In the lower region the upward velocity is at maximun about half of the jet velocity. This motion is the fluid flowing from the node towards the jet trajectory. Yuan et al. found that at $Re_D = 2100$ there was a clear distinction between the sign of the vertical vorticity emerging from the left-hand side and the right-hand side of the pipe [13]. This notion is confirmed in this case. The vorticity seems to mix quicker in the present case, which is probably due to the higher Reynolds number. Figure 4 reveals the vortices with the isosurface of the second invariant of the velocity gradient Q defined as

$$Q = -\frac{1}{2}(\overline{S}_{ij}\overline{S}_{ij} - \overline{\Omega}_{ij}\overline{\Omega}_{ij}) = -\frac{1}{2}\frac{\partial \overline{u}_i}{\partial x_j}\frac{\partial \overline{u}_j}{\partial x_i}$$

An animation shows that the vortex upstream of the jet exit is formed and it moves to the lip of the jet exit where it seems to merge with the vortices of opposite sign rising from the pipe. The merger may explain that at a distance of approximately one diameter after the exit there is weaker coherent vorticity in front of the jet. The resolved turbulent kinetic energy (TKE) in the symmetry plane (Fig 5) shows a maximum under the jet

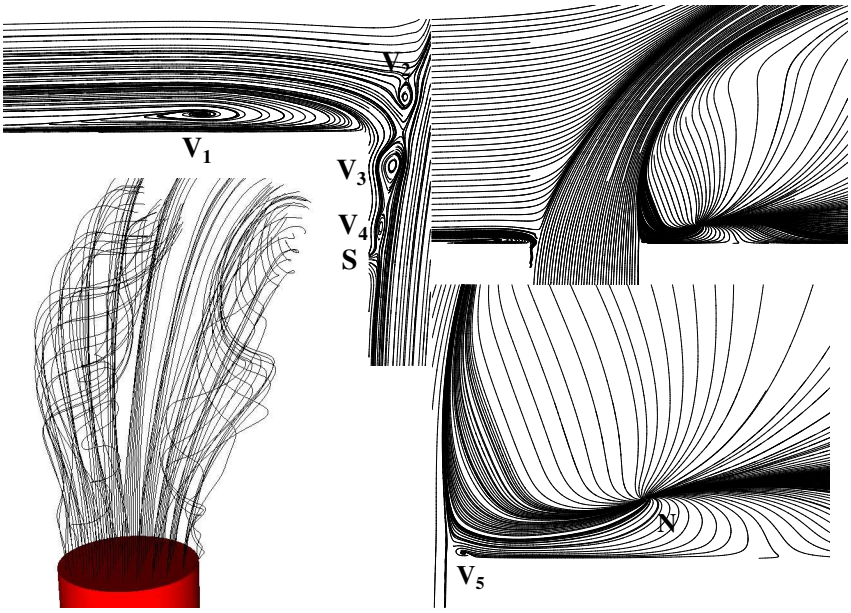

Figure 2: The streamlines of the mean velocities in the symmetry plane in the right upper corner. A magnification upstream from the jet exit is located in the left upper corner. The lee of the jet is magnified in the lower right corner. Three-dimensional streamlines emerging from the pipe are shown in the left lower corner.

trajectory where the flow emerging from the node curves to join the jet. Another smaller maximum is located at the node behind the jet. The eddy viscocity (Fig 5) exhibits the maximum in the same location as TKE. At the node there is no maximum. This is prevented by a shorter length scale due to the grid clustering or a smaller strain rate, or both. The greatest viscocity ratio, approximately 35, exists in the shear layer of the inlet pipe. As the resolved TKE is almost zero there the subgrid scale viscocity acts more like a Reynolds-averaged model in that region. Poor accuracy is obtained inside the pipe but this is not important in the simulation of the jet, which is the primary focus of the present work.

5.2 Comparison to the Measurements

A comparison of the calculated flow field to the experiment of Crabb, Durão and Whitelaw (CDW) is conducted next. The mean streamwise velocities in the central plane are shown in Fig 6. At x/D =-1 the present LES shows a peak of velocity near the flat wall, which is due to the vortex blocking the flow. CDW shows no such peak. At the dowstream pipe wall $x/D = 0.5$ the LES predicts a small backflow, which becomes stronger especially close to the wall. There are two minima seen in the backflow at $x/D = 0.75$ and 1. The strong backflow near the wall nodes might be a sign of a non-physical phenomenon owing to too coarse cells for the present wall-resolved LES. Andreopoulos

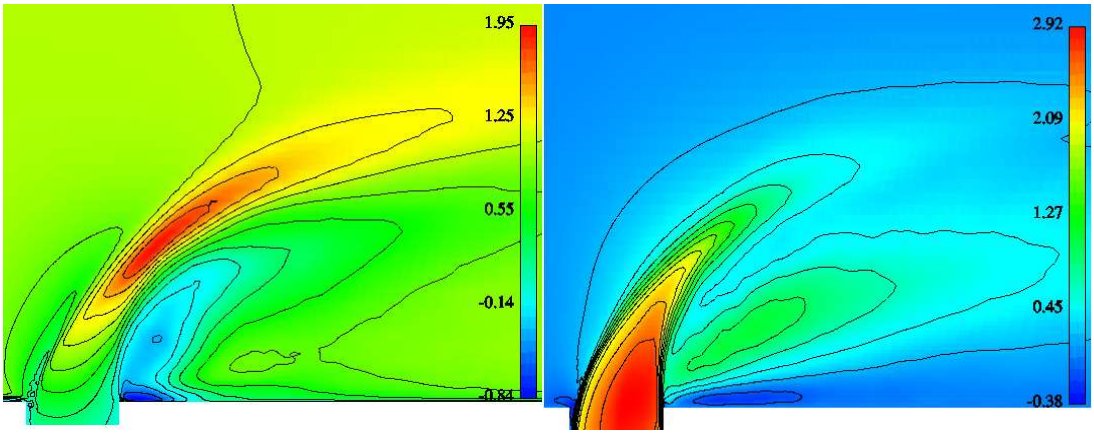

Figure 3: Mean streamwise velocity U/U_∞ and vertical velocity V/U_∞ contours in the symmetry plane.

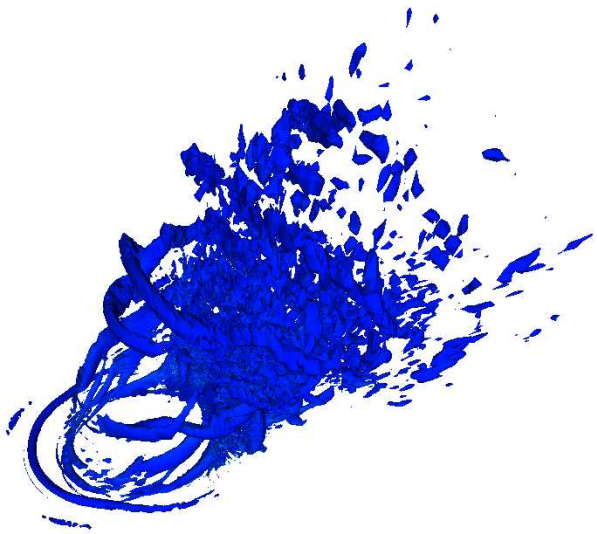

Figure 4: An instantaneous isosurface of the second invariant of the velocity gradient $Q = 30$.

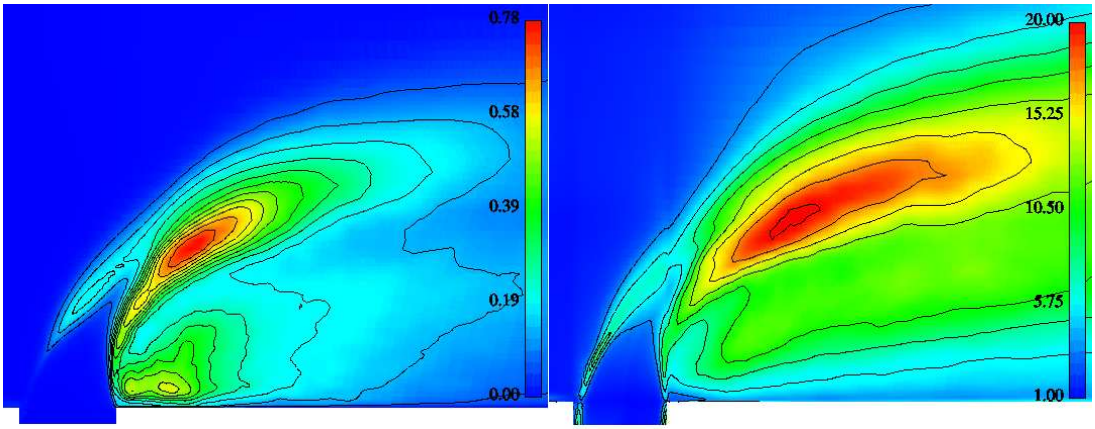

Figure 5: Turbulent kinetic energy $\frac{\overline{u_i' u_i'}}{2U_\infty^2}$ and eddy viscocity $\frac{\overline{\nu + \nu_{sgs}}}{\nu}$ contours in the symmetry plane.

and Rodi [1] mention that in the lee of the jet with similar parameters, a rewerse-flow region forms very close to the wall in which measurements were not possible.

In CDW the backflow resides approximately between $x/D = 0.75$ and 3; no backflow near the wall can be deduced from CDW. In the LES there is no backflow downstream of $x/D = 2$ and the flow profile is flatter than that of CDW. Figure 8 shows the streamwise velocities plotted at various distances y/D from the wall and z/D from the central plane. This plot confirms clearly the previous conclusion. The LES predicts the backflow too close to the wall and to the jet exit.

In the LES the streamwise turbulent intensity (Fig 7) upstream of the jet is lower than in CDW, which is probably due to the steady inlet condition. This hardly affects the result in the jet region as the incoming intensity is rather low and at the jet exit the profiles are quite consistent. Downstream of the inlet there are two maxima in the intensity profile. They reside approximately at the location of the steepest gradient of the velocity. In general, the turbulent intensities are rather well predicted compared to the mean velocity.

Figures. 8 and 9 show the streamwise and wall-normal velocities plotted along lines at various distances y/D from the wall and z/D from the central plane. The LES predicts the location of the backflow closer to the jet exit and closer to the wall than the measurements indicate (Fig. 8, $z/D = 0$). The jet profile has an approximately 10 % higher peak value than the measured one at $y/D = 0.25$ (Fig. 9, $z/D = 0$). Crabb et al. report that the profile at the outlet is a fully developed profile in a pipe whose length was 30 D. In the present LES a steady mean profile was set at the inlet. Yuan et al. performed simulations to experiment with the effect of different inlet conditions [13]. They tested with a plug flow profile, a mean turbulent profile and a temporally evolving pipe and reported that the latter boundary condition improved obviously the result. However, the evidence they

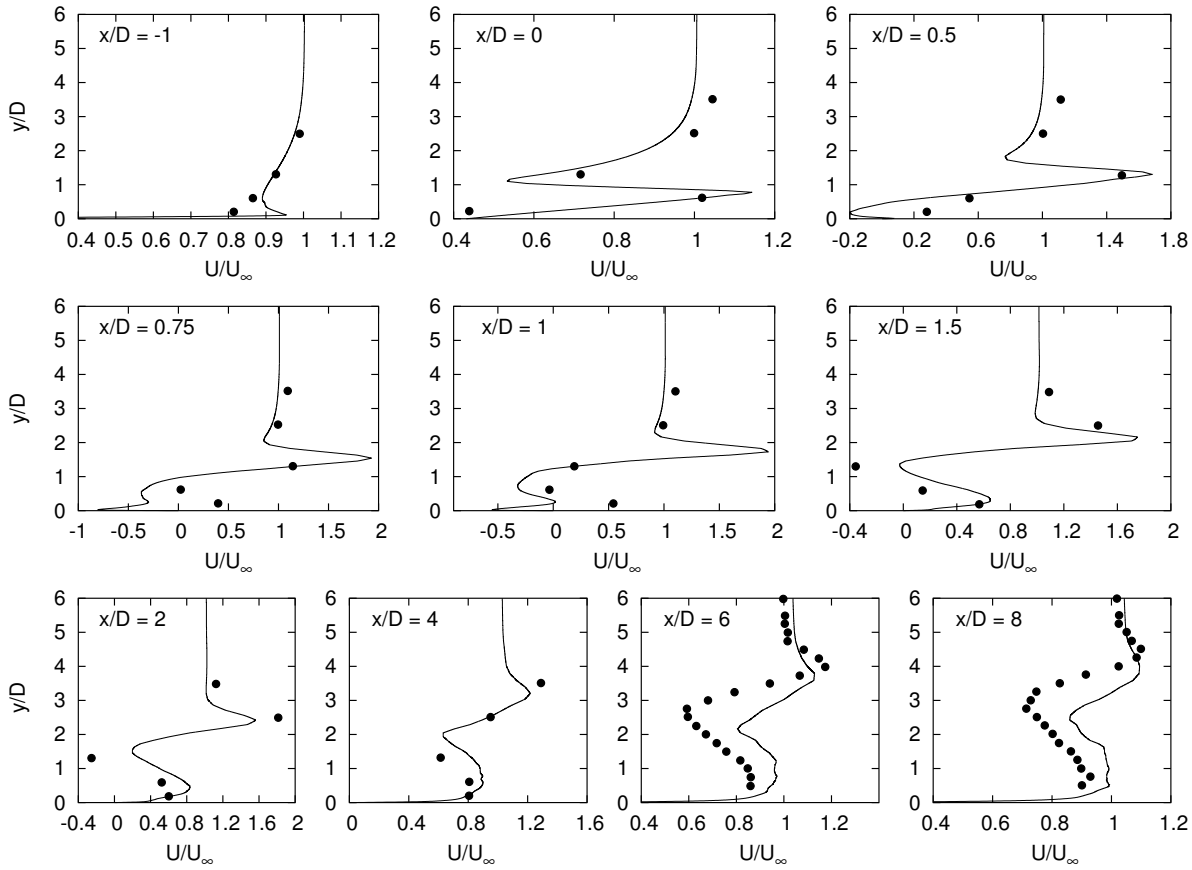

Figure 6: Mean streamwise velocities in the central plane, $z/D = 0$. The solid curve stands for the LES result and the symbol • stands for the measurements of Crabb et al. [3].

provide to support this conclusion does not convince the present authors. Wille set the boundary condition at the wall by setting the lateral components to zero and the vertical component to such a value that the mean dynamic pressure was constant [12]. This condition produced a surprisingly good agreement with CDW at $y/D = 0.25$ although it prevents any interaction of the colliding flows inside the pipe. The high velocity behind the jet indicates again the short distance to the node.

Further up at $y/D = 2.5$ the jet has lost momentum since both streamwise and vertical velocities are underpredicted. The jet has probably spread in the spanwise direction as the momentum deficit is smaller at $z/D = 0.5$ than in the symmetry plane in Fig. 8.

In the LES the streamwise turbulent intensity (Fig. 10) upstream of the jet is lower than the measured one, which is again probably due to the steady inlet condition. In general the turbulent intensities are rather well predicted compared to the mean velocity. Far from the symmetry plane the computed turbulent intensity is smaller in the simulation especially close to the wall ($z/D = 1.5$, $y/D = 1.35$). The Smagorinsky model without any

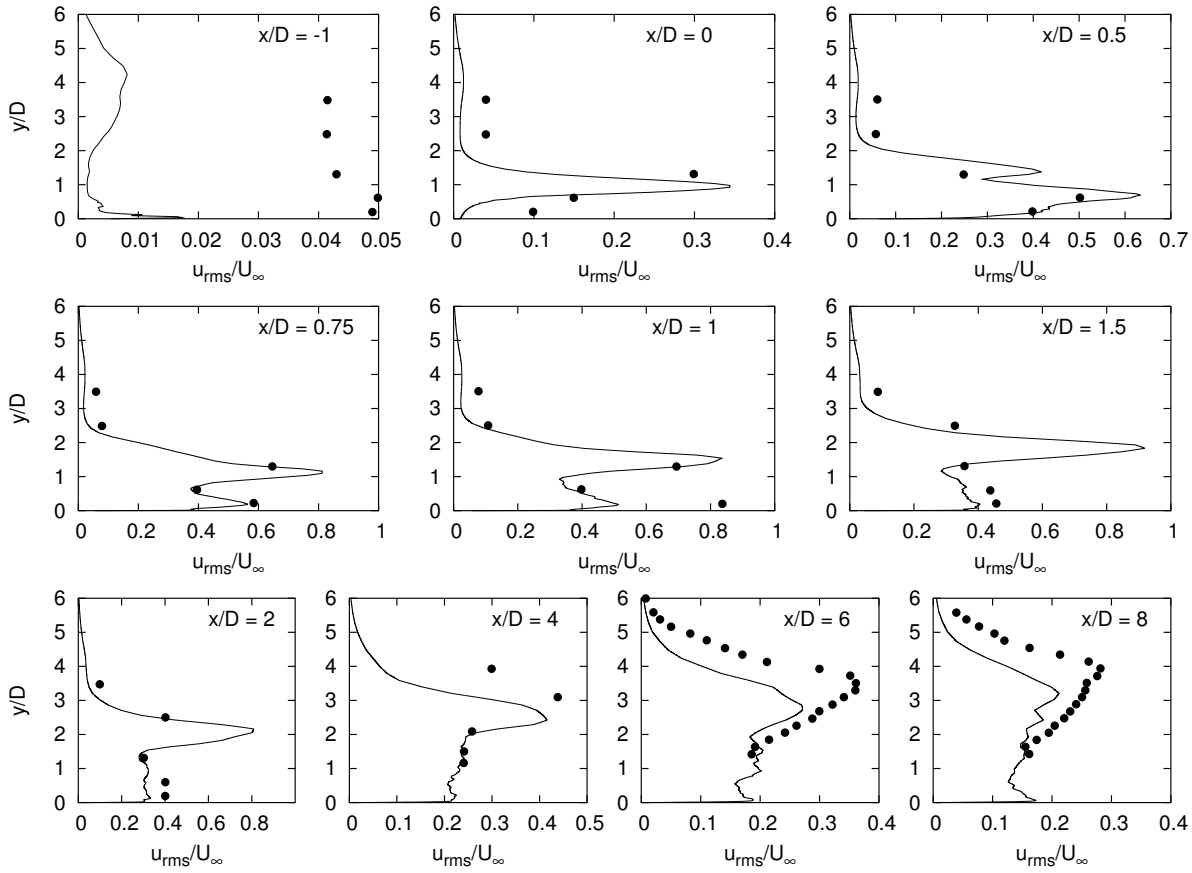

Figure 7: Streamwise turbulence intensities in the central plane, $z/D = 0$. The solid curve stands for the LES result and the symbol • stands for the measurements of Crabb et al. [3].

damping for the length scale near the wall may be the reason for this. The wall-normal turbulent intensity (Fig. 11) shows two distinct peaks near the jet exit, corresponding to the upstream and downstream shear layers of the pipe flow. Close to the wall ($y/D = 0.25$) the LES predicts a very small intensity on the upstream side, probably owing to the steady inlet condition in the jet. In the lee of the jet the intensities are in a reasonable agreement with CDW. The backflow generates fluctuations close to the wall, and on the upstream side the fluctuations grow closer to the measured ones further up, which is probably connected to the development of the ring vortices. In Figures 10 - 11 there are plots also of the total stresses including the contributions from the subgrid-scale model. Only the anisotropic part is included as the isotropic part of the stress is lumped into the pressure. It is hard to distinguish the two quantities from each other, only near the vicinity of the jet exit there is a small difference in the shear stresses $\overline{u'v'}$ and $\overline{u'v' + \tau_{12}^a}$ (not shown). Wille observed differences in the resolved and the total stresses with a coarse grid (88440 cells) but the differences are reported to be very small with the fine

mesh (997920 cells) [12]. As Wille stated, near the shear layers the modelled stress might be significant. The highest eddy viscocity of approximately 35 is calculated near the pipe wall where there is little or no resolved turbulence, as shown by Fig. 5.

Figure 12 presents lateral profiles for the plane $X/D = 8$. The simulated jet has dispersed there as the profile has become flatter than the measured one, which is seen also in Fig. 6. The Reynolds stresses are rather isotropic. In [3] there are some unclear plots, especially concerning normal stresses at $y/D = 1$, which might explain most of the differences seen between the present LES and the measured results. Considering the coarse mesh in the far field and the short sampling time, the cross stresses $\overline{u'v'}/U$ and $\overline{u'w'}/U$ are relatively well predicted. At $y/D = 1$ and 4, the measured $\overline{u'w'}/U$ is negative at the centre plane, although it should be zero, on the grounds of symmetry arguments. Either there must be an asymmetry in the flow or the measurement itself is in error.

5.3 Scalar Mixing

In a preliminary calculation with a lower Reynolds number it was observed that the central difference led into spurious wiggles in the scalar field. The computed mixture fraction had values lower than zero and higher than one. This was observed also by Wille who thought that using a TVD scheme would be unacceptable for excessive smearing [12]. In the mean mixing fraction the spurious values were averaged off mostly. In preliminary tests a TVD-limited central difference for scalar in the convection term reduced overshoots effectively, but not completely. Here a MUSCL scheme is used with the minmod limiter [5]. With the central difference discretization the variables extrapolated at the cell face $i + \frac{1}{2}$ from left- and right-hand side are

$$\theta^L_{i+\frac{1}{2}} = \theta_i + \frac{1}{2}\phi(r^-_{i+\frac{1}{2}})(\theta_{i+1} - \theta_i) \tag{10}$$

$$\theta^R_{i+\frac{1}{2}} = \theta_{i+1} - \frac{1}{2}\phi(r^+_{i+\frac{1}{2}})(\theta_{i+1} - \theta_i), \tag{11}$$

where the minmod limiter is defined as

$$\phi(r) = \min(r, 1) \quad , \quad r > 0$$
$$\phi(r) = 0 \quad , \quad r \leq 0$$

and the arguments of the limiter are the ratios of the consequent variables

$$r^-_{i+\frac{1}{2}} = \frac{\theta_i - \theta_{i-1}}{\theta_{i+1} - \theta_i} \qquad r^+_{i+\frac{1}{2}} = \frac{\theta_{i+2} - \theta_{i+1}}{\theta_{i+1} - \theta_i}.$$

If the limiter is activated the discretization becomes upwind-biased and numerical dissipation is introduced. In the present case a mixture fraction was restricted to lie between 0 and 1, otherwise solution diverged in time. This was the case both in TVD-limited

and unlimited case. Fig. 13 shows the mean mixture fraction in the central plane. The TVD-limited scalar does not spread as much as the non-limited scalar. Both schemes underestimate the spreading under the jet. The non-limited scalar fluctuates more than the limited scalar which explains the differences in the spreading. The schemes showed no clear difference in magnitudes in a streamwise turbulent scalar transport. In other directions the transport terms were not recorded. The contour plot Fig. 14 shows that in the measured flow (solid contour lines) the rich helium concentration does not coincide with the maximum velocity in the far field plane at $x/D = 8$. The flow with higher momentum thus originates from the free-stream fluid accelerated around the jet. The simulated velocity is flatter on the whole plane, as also seen in Fig 6. The simulated mixture fraction shows a better agreement with the experiment than the velocity field.

6 CONCLUSIONS

The LES of a turbulent jet in a crossflow with the present Reynolds number is an expensive computation. The domain contained 2 764 800 control volumes, which were divided equally between 25 processors. The computation in which the crossflow advanced 10.2 times through the domain took approximately 40 days in calendar time when 25 Power4 processors were applied.

Many issues in the present study were unexplored due to the huge computer cost. The effect of different boundary conditions is one of them. In the present study steady conditions were used at the inlet and it might be valuable to test with inlet conditions that evolve in time. The dynamic model did not stabilize the present case enough and the calculation diverged soon if the model was applied. The flow was resolved to the wall with no wall modelling. The Smagorinsky model was applied with no length scale damping near walls. In major part of the domain the modelled stresses are negligible compared to the averaged resolved ones. However, the resolved stresses consist of the large scale motion, and the modelled stress is significant in stabilizing the calculation. In the shear layers (e.g. in the inlet pipe) the modelled stresses might be large even if compared to the resolved stress. As the resolved stress is very small there, the subgrid scale model works as a Reynolds-averaged model. The resolution near the walls may be too coarse for the LES performed here.

The computation reproduced many phenomena present in such a flow, like the shear layer ring vortices. In general, a reasonable agreement with the measurements was obtained. The LES predicts the backflow too low near the flat wall and too close to the jet which is the most significant deviation from the measurements

Acknowledgements

This research project has been funded by the Ministry of Education through Graduate School in CFD and National Technology Agency of Finland TEKES. Also CSC, the Center of Scientific Computation, is acknowledged for providing the IBM cluster.

REFERENCES

[1] J. Andreopoulos and W. Rodi. Experimental investigations of jets in a crossflow. *Journal of Fluid Mechanics*, 138:93–127, 1984.

[2] W. Cabot and Parviz M. Large eddy simulation of scalar transport with the dynamic subgrid-scale model. In Galperin B. and Orszag S.A., editors, *Large Eddy Simulation of Complex Engineering and Geophysical Flows*, chapter 7, pages 141–158. Cambridge University Press, Cambridge, UK, 1993. ISBN 0–521-43009-7.

[3] D. Crabb, D.F.G Duráo, and J.H. Whitelaw. A round jet normal to a crossflow. *Transactions of the ASME: Journal of Fluids Engineering*, 103:568–580, 1981.

[4] J.W. Deardorff. A numerical study of three-dimensional turbulent channel flow at large Reynolds numbers. *Journal of Fluid Mechanics*, 41:453–480, 1970.

[5] Charles Hirsch. *Computational Methods for Inviscid and Viscous Flows*, volume 2 of *Numerical Computation of Internal and External Flows*. John Wiley & Sons Ltd, Chichester, 1990. ISBN 0–471–92351–6.

[6] J.F. Keffer and W.D. Baines. The round turbulent jet in a cross-wind. *Journal of Fluid Mechanics*, 15:481–497, 1963.

[7] R.M. Kelso, T.T. Lim, and A.E. Perry. An experimental study of round jets in cross-flow. *Journal of Fluid Mechanics*, 306:111–144, 1996.

[8] P. Majander. Deveplopments in large eddy simulation. Report 128, Helsinki University of Technology, 2000. ISBN 951–22–4861–1.

[9] P. Majander and T. Siikonen. Large Eddy Simulation of a Round Jet in a Crossflow. Report 142, Helsinki University of Technology, 2003. ISBN 951–22–6742–X.

[10] P. Majander and T. Siikonen. A parallel multi-block Navier-Stokes solver for large-eddy simulation in complex flows. In *VIII Suomen mekaniikkapäivät*, pages 395–406, Espoo, Finland, Jun 2003. TKK.

[11] J. Smagorinsky. General circulation experiments with the primitive equations, part I: The basic experiment. *Montly Weather Review*, 91:99–152, 1963.

[12] M. Wille. *Large Eddy Simulation of jets in cross flows*. Ph.d. thesis, Imperial College of Science, Technology and Medicine, Department of Chemical Engineering, London, Sep 1997.

[13] L.L Yuan, R.L. Street, and J.H Ferziger. Large-eddy simulations of a round jet in crossflow. *Journal of Fluid Mechanics*, 379:71–104, 1999.

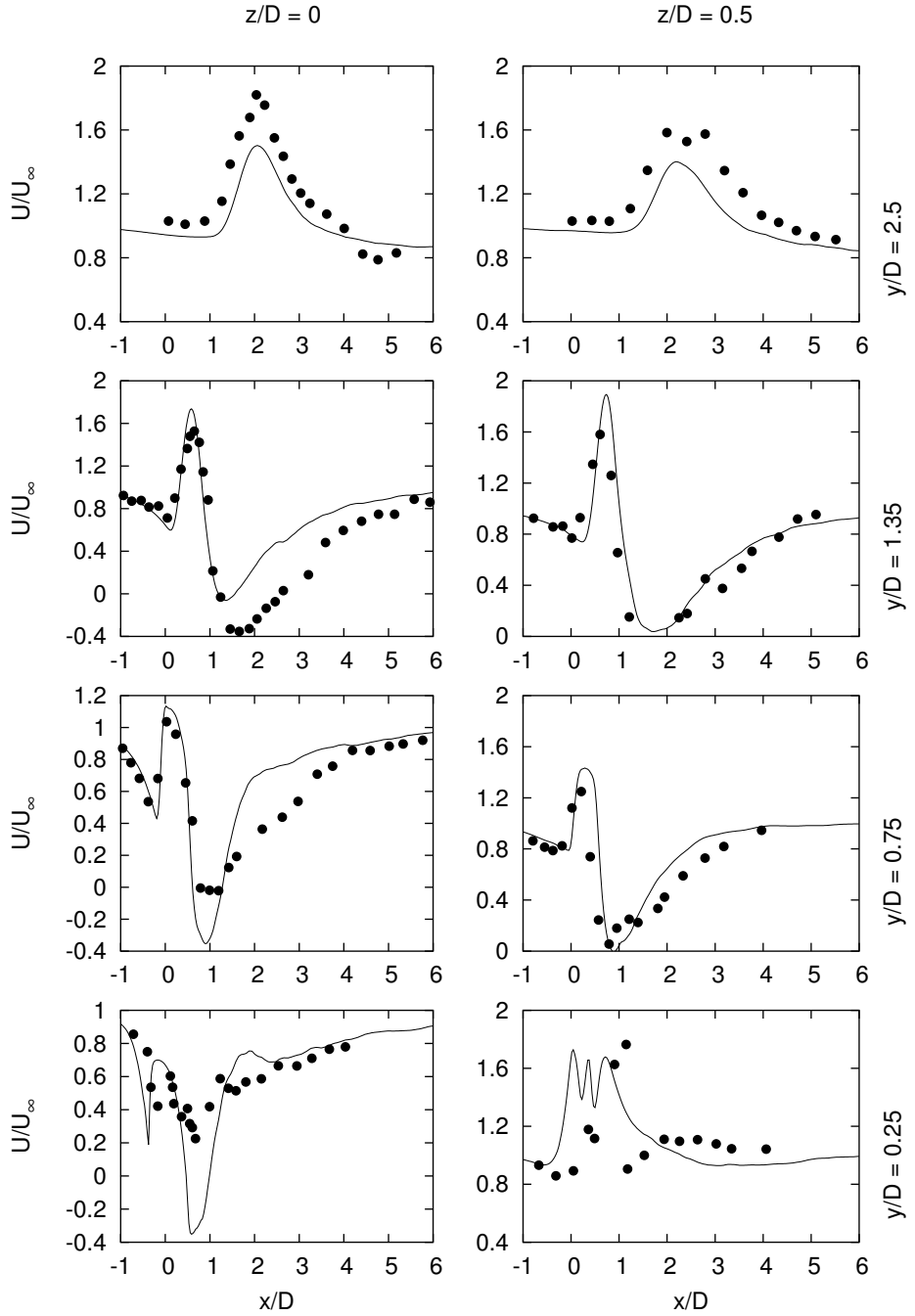

Figure 8: Mean streamwise velocities plotted at various distances y/D from the wall and z/D from the central plane. The solid curve stands for the LES result and the symbol • stands for the measurements of Crabb et al. [3].

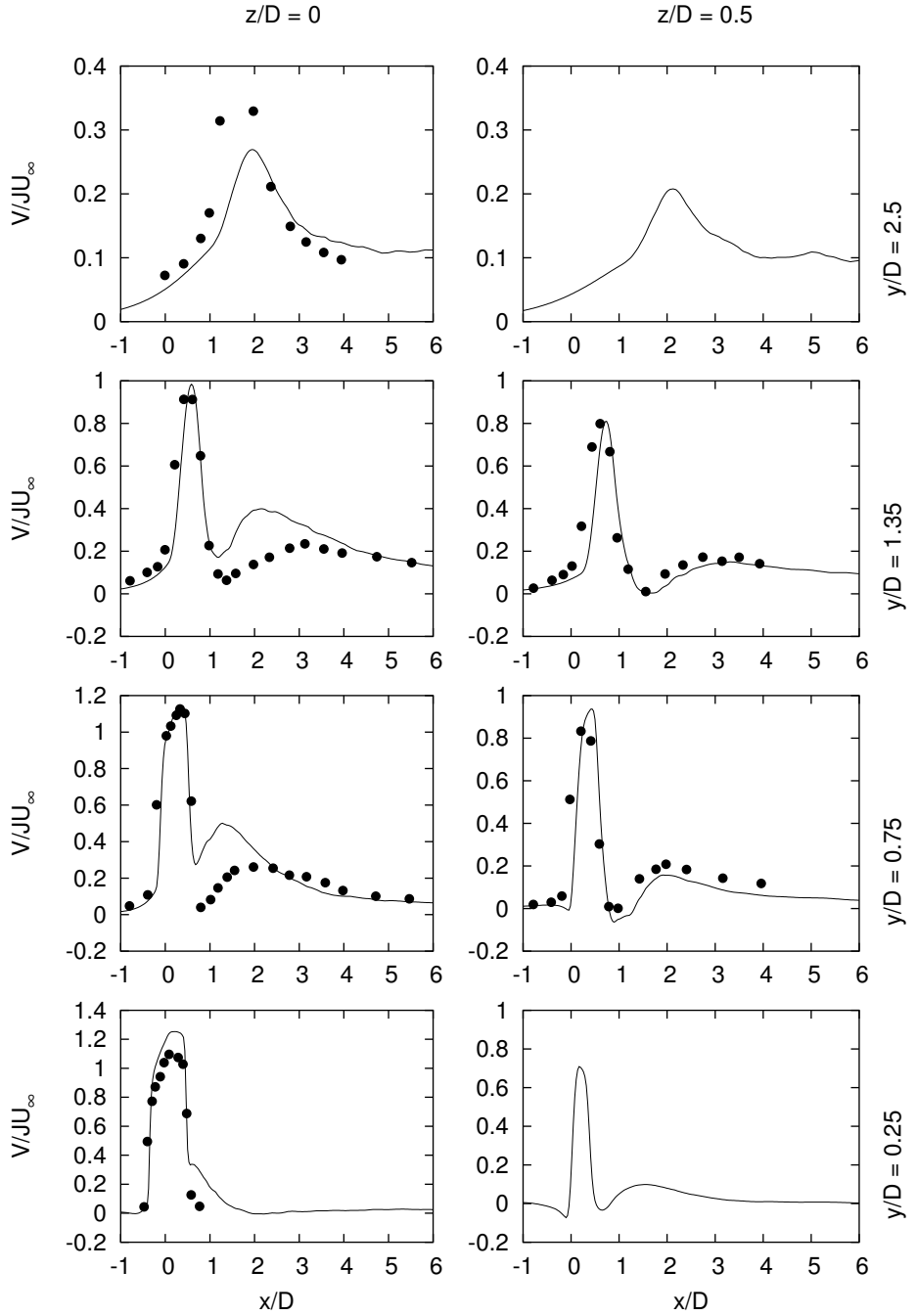

Figure 9: Mean wall-normal velocities plotted at various distances y/D from the wall and z/D from the central plane. The solid curve stands for the LES result and the symbol • stands for the measurements of Crabb et al. [3].

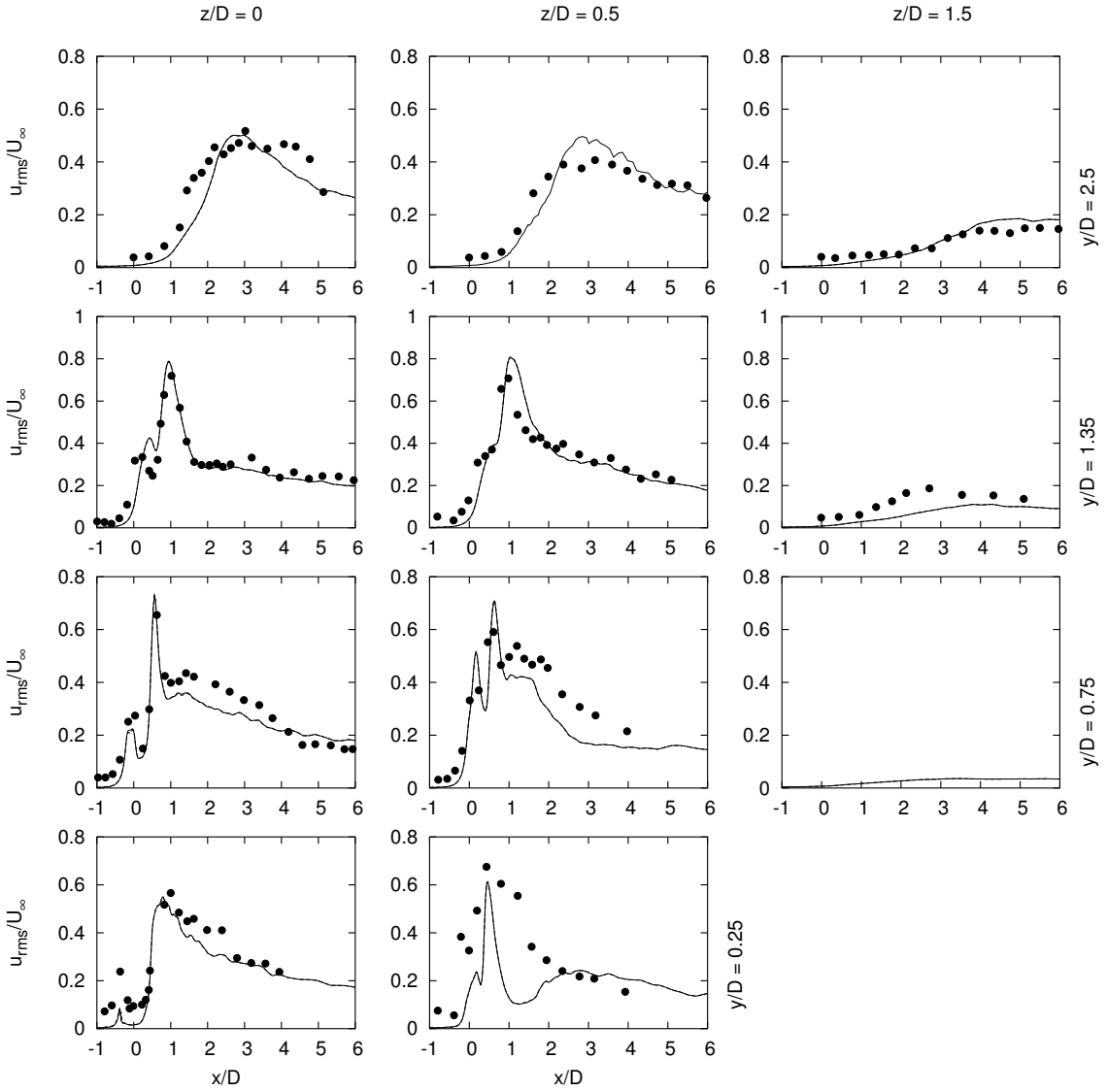

Figure 10: Streamwise turbulence intensities plotted at various distances y/D from the wall and z/D from the central plane. The solid curve stands for the resolved v_{RMS}, the dotted curve for $[u + \tau^a_{11}]_{RMS}$ and the symbol • for the measurements of Crabb et al. [3].

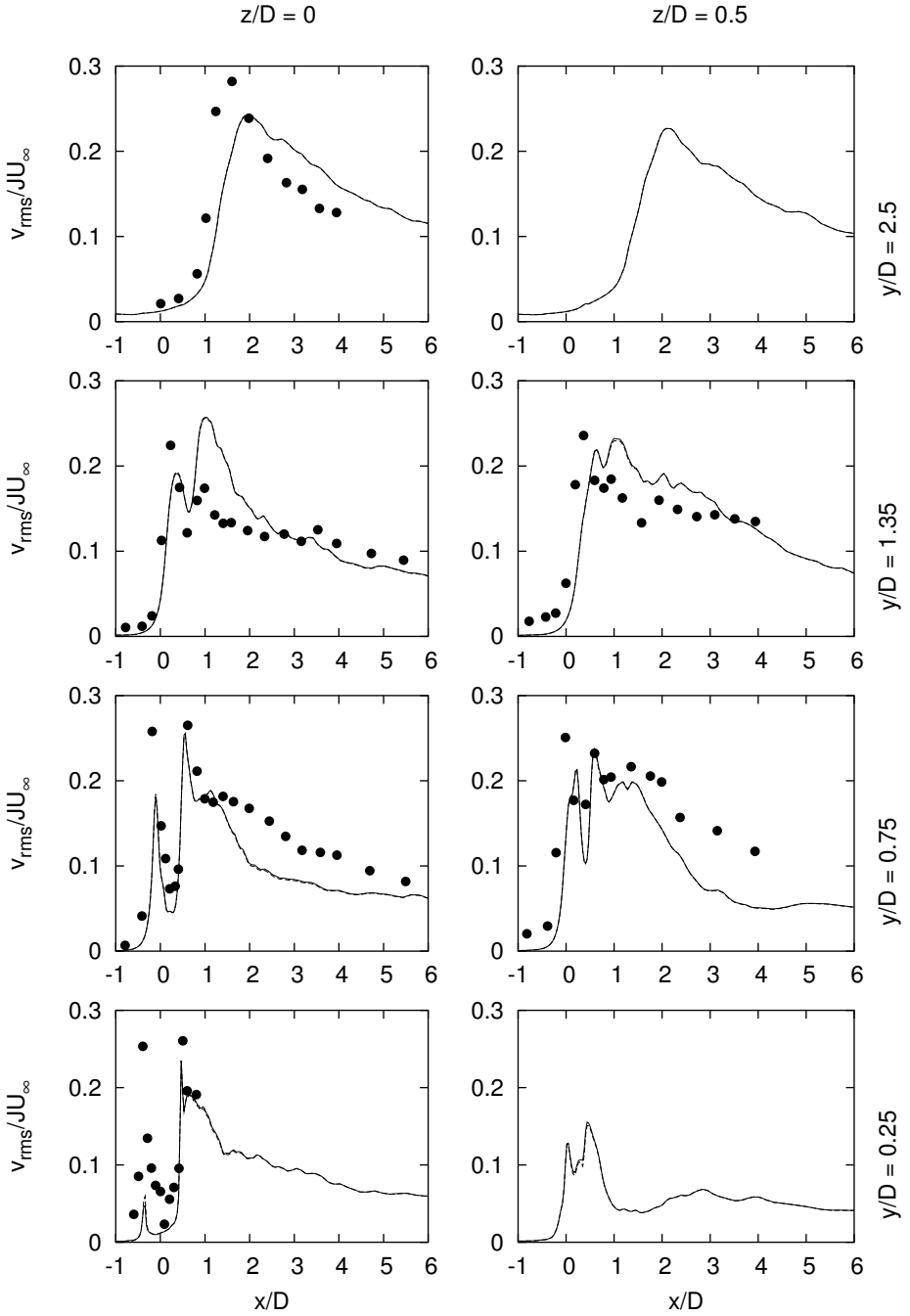

Figure 11: Wall-normal turbulence intensities plotted at various distances y/D from the wall and z/D from the central plane. The solid curve stands for the resolved v_{RMS}, the dotted curve for $[v + \tau_{22}^a]_{RMS}$ and the symbol • for the measurements of Crabb et al. [3].

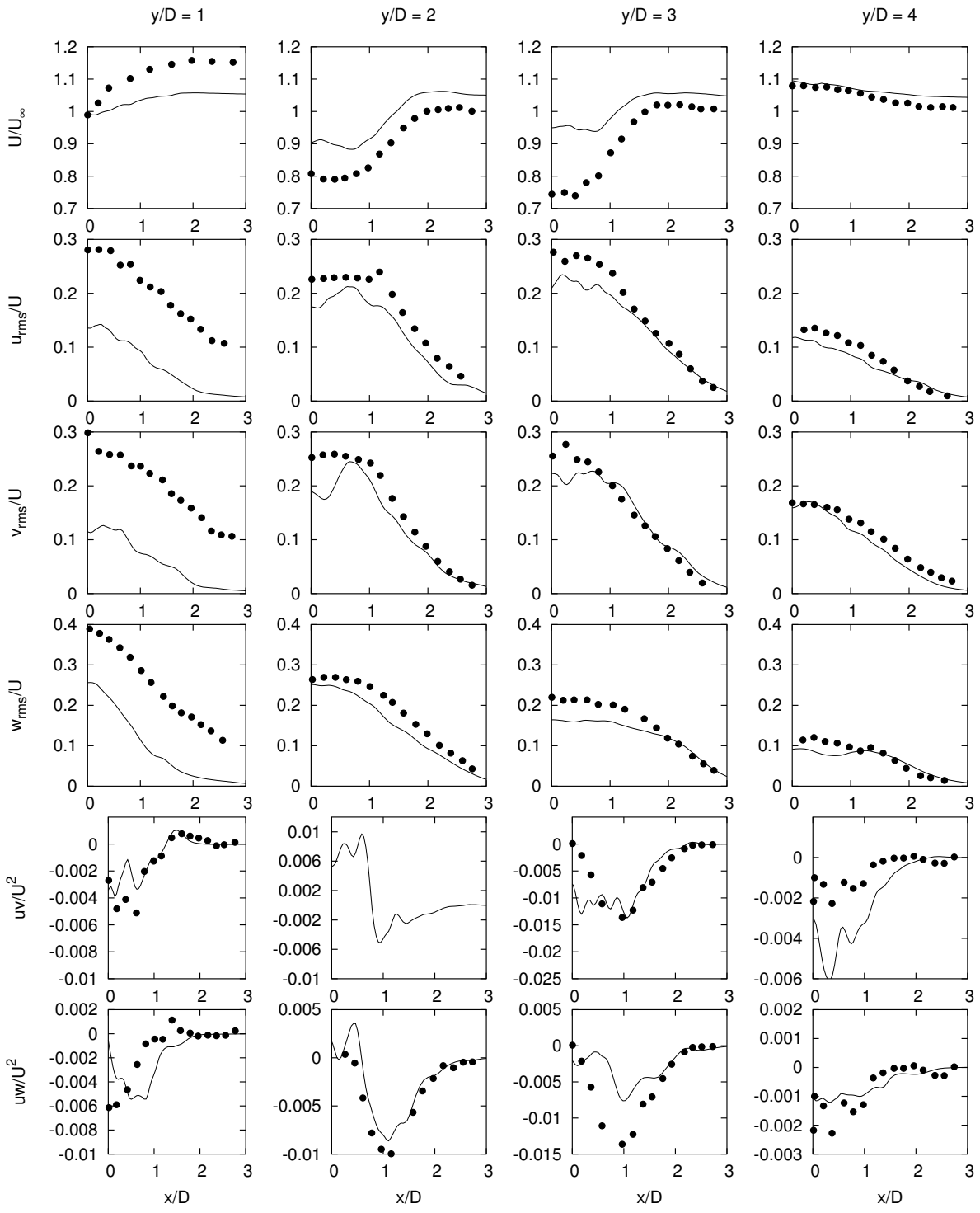

Figure 12: Mean velocity and Reynolds stress profiles at the position $x/D = 8$ at various distances y/D from the wall and z/D from the central plane. The solid curve stands for the LES result and the symbol • stands for the measurements of Crabb et al. [3].

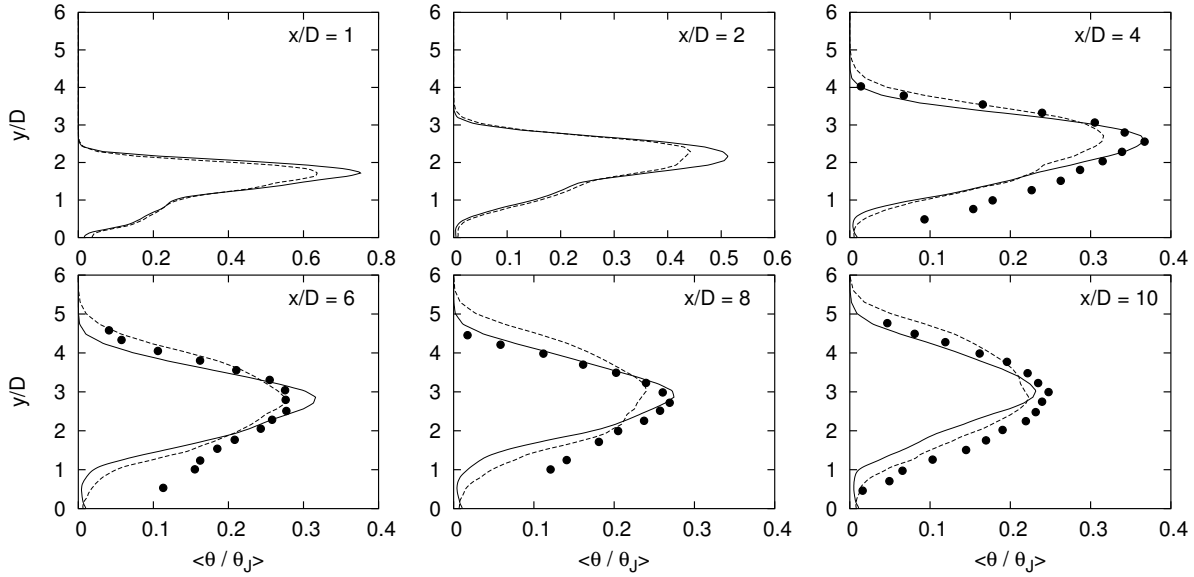

Figure 13: Mean mixture fraction in the central plane, $z/D = 0$. The solid curve stands for the LES scalar result with the minmod limiter and the dashed curve without any limiter. The symbol • stands for the measurements of Crabb et al. [3].

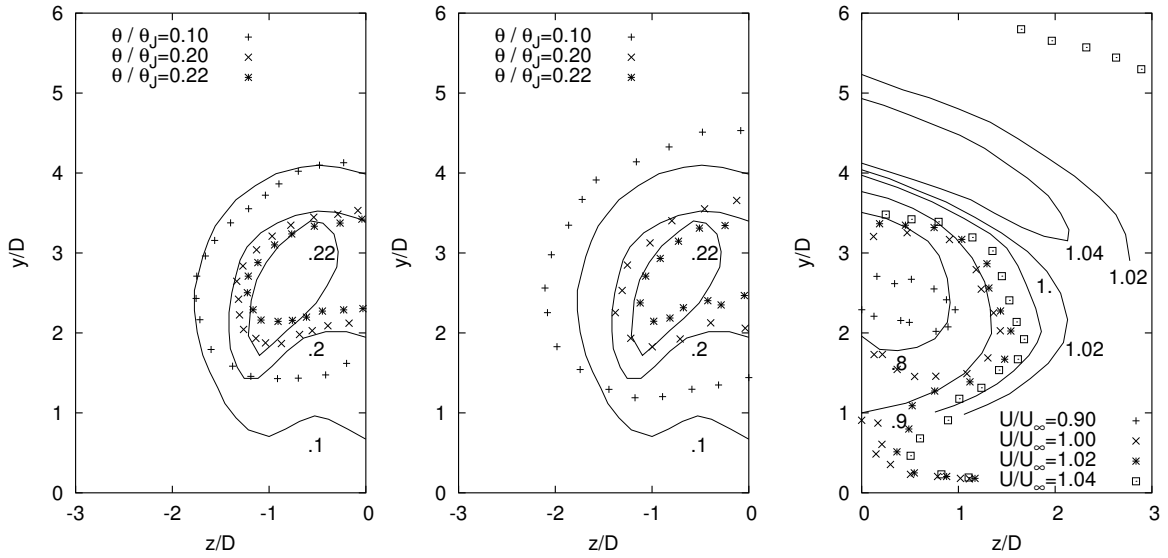

Figure 14: Contours of the mixture fraction and the mean streamwise velocity in the plane, $x/D = 8$. The TVD-limited result on the left, the non-limited result in the centre and the velocity on the right. The solid curves stand for the measurements of Crabb et al. [3].